Received: 23 August 2021 | Revised: 28 June 2022 | Accepted: 9 July 2022 | Published on: 26 July 2022

DOI: 10.1002/joc.7802

RESEARCH ARTICLE

International Journal of Climatology RMetS

# A climatology of aerosol optical depths in the ultraviolet wavelengths for Hobart, Australia, as determined by a Brewer MKIII spectrophotometer

**Manuel Nuñez**[1] | **Antonio Serrano**[2] | **Nels R. Larson**[3]

[1]Geography and Spatial Sciences Discipline, College of Science and Engineering, University of Tasmania, Hobart, Tasmania, Australia

[2]Departamento de Fisica, Facultad de Ciencias, Universidad de Extremadura, Badajoz, Spain

[3]Albireo Endeavors, Shingletown, California, USA

**Correspondence**
Manuel Nuñez, Geography and Spatial Sciences Discipline, College of Science and Engineering, University of Tasmania, Sandy Bay, Hobart, TAS 7005, Australia.
Email: m.nunez@utas.edu.au

**Funding information**
Australian Bureau of Meteorology; Consejería de Educación y Empleo, Junta de Extremadura, Grant/Award Number: MOV15B036; MCIN/AEI, Grant/Award Number: RTI 2018-097332-B-C22

**Abstract**

The study examines aerosol optical depth (AOD) measurements at 320 nm wavelength by a Brewer MKIII spectrophotometer located in Hobart, Australia. A climatology was developed from records encompassing the period April 4, 2002, to February 27, 2019. A methodology is described to extract cloudless episodes and cloudless half-days. Extraterrestrial irradiances are obtained using a travelling calibration standard and are supplemented by Langley analyses on cloudless and stable half-days. AODs are obtained by applying Beer's law to every reading and subtracting known values of ozone optical depth and Rayleigh scatter. Statistics are provided on the daily, monthly and interannual variability. Concurrent measurements from a Multi-filter Rotating Shadowband Radiometer (MFRSR) operating in the visible band enabled the spectral variability of AOD to be determined. They showed the dominance of oceanic aerosols but with some input from land-based aerosols originating mostly from biomass burning.

**KEYWORDS**

aerosol optical depth, Brewer, UV wavelengths, observational data analysis, geophysical sphere, physical phenomenon, atmosphere, physical phenomenon, radiation, scale, aerosols, tools and methods, climate

## 1 | INTRODUCTION

Aerosols presently provide the largest uncertainty in model estimates of climate change, and furthermore, they directly affect human health and can negatively affect the physical environment (WMO, 2014; IPCC, 2021). Presently there are several global networks of stations that measure extinction of solar radiation by aerosols using sun photometers, such as the Aerosol Robotic Network (AERONET; Holben *et al.*, 2001) and SKYNET (Nakajima *et al.*, 2020). In the ultraviolet range, the Brewer spectrophotometer network offers an added source of aerosol information on a global scale as there are approximately over 150 operational Brewer stations around the world acquiring ozone and spectral ultraviolet radiation data (https://woudc.org). Many studies provide aerosol optical depth (AOD) from Brewer data in a variety of environments covering mostly northern hemisphere urban regions. The procedure usually involves using direct solar irradiance observations from the Brewer instrument and applying Beer's law (Carlund *et al.*, 2017; Kumharn *et al.*, 2012; De Bock *et al.*, 2010; Kazadzis *et al.*, 2007; Sellito *et al.*, 2006;

Gröbner and Meleti, 2004; Marenco *et al*., 2002; Carvalho and Henriques, 2000).

High aerosol loads are infrequent in the Australian region, but dust events are common (Alizadeh-Choobari *et al*., 2013). In this study, we examine AOD in Hobart, Australia, a rural and largely pristine region of the southern hemisphere located in the island State of Tasmania (Figure 1). Our method applies the methodology developed by Smirnov *et al*. (2000) for AERONET data, and Gröbner and Meleti (2004), De Bock *et al*. (2010), and Diemoz *et al*. (2016) for Brewer data. The approach essentially filters out cloud effects using various criteria that include examining Brewer Direct Sun (DS) records and their standard deviations during the instrument's five repetitive cycles (see next section).

Variability of AOD in the visible/UV range is also examined using a Multifilter Rotating Shadowband Radiometer (MFRSR), which was operational at the study site during part of the Brewer collection period. The MFRSR instrument has been extensively used to provide AODs in the visible solar spectrum (see for example Harrison *et al*., 1994; Harrison and Michalsky, 1994; Hallar *et al*., 2015; Sanchez-Romero *et al*., 2016).

The manuscript is partitioned into the following sections. After the *Introduction* (Section 1) follows the *Methodology* (Section 2), which provides details of the Brewer and MFRSR instruments, site characteristics, data acquisition, and the physical model. In *Data Processing and Analysis* (Section 3), we describe the data processing steps, determination of absorption and scattering coefficients, determination of the extraterrestrial irradiance and the uncertainty analysis. The *Results* (Section 4) presents statistics of AODs and their temporal and spectral variability. The *Discussion and Conclusion* (Section 5) finalizes the study.

## 2 | METHODOLOGY

### 2.1 | Instrumentation

A double-grating Brewer MKIII spectrophotometer #179 (Kipp and Zonen, 2014) was purchased in 2002 and has been operational from April 2002 up to the present. The instrument acquires direct spectral irradiance in five distinct wavelength bands when operating in DS mode

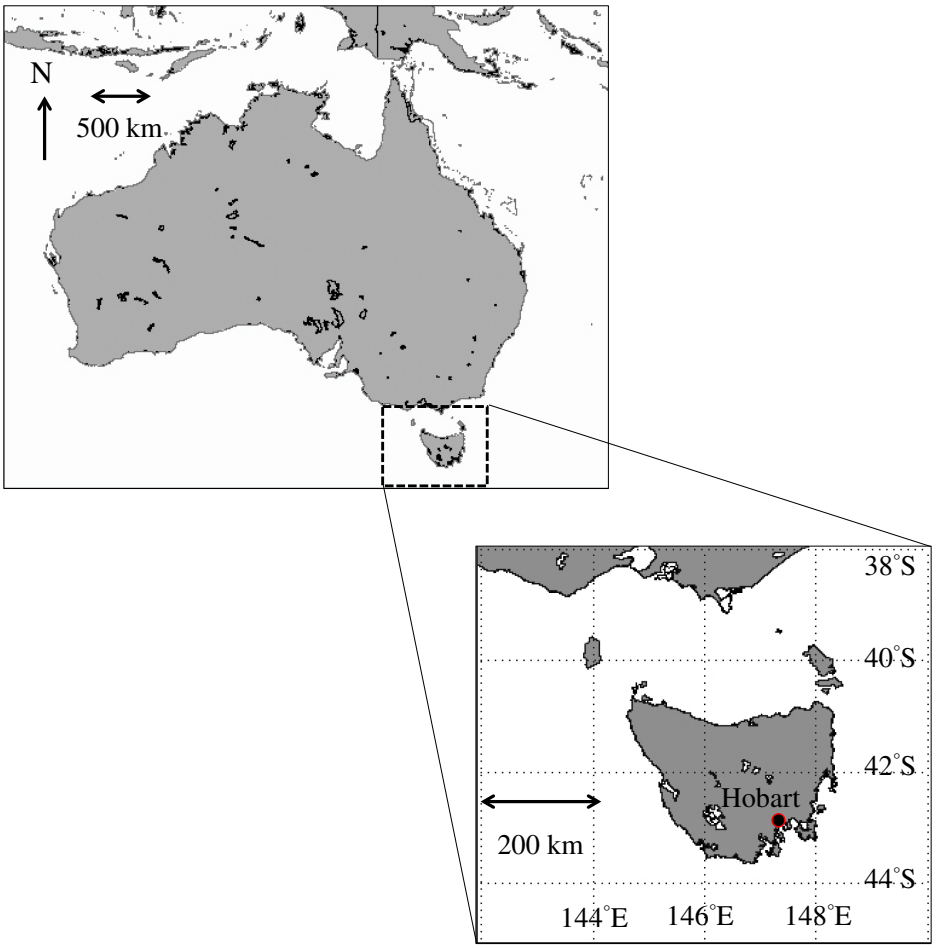


**FIGURE 1** Location of the Brewer #179 in Hobart, Australia. Site coordinates are 42.8806°S, 147.3250°E [Colour figure can be viewed at wileyonlinelibrary.com]

(306.13, 310.03, 313.50, 316.79, 319.96 nm with a 0.5 nm FWHM). These data are routinely processed to obtain column ozone. The solar tracker and collimating system captures direct solar radiation which is channelled into the fore-optics, transmitted by a filter assembly, and diffracted by two holographic gratings with a slit mask into the above wavelengths. A set of five measurements (five readings at five wavelengths) determines a complete DS cycle with a resultant column ozone measurement. The frequency of sampling is determined by a user-defined schedule list to optimize ozone information.

The system is maintained following the usual procedures, including regular cleaning of the quartz window and dome several times a week, checking SL and HG tests, replacement of the internal mercury and tungsten lamps when required, voltage checks using AP tests, humidity checks, dead time checks, and occasional cleaning of the azimuth tracker (Kipp and Zonen, 2014; McElroy, 2008). The power supply had to be replaced on three occasions as it was not able to provide a constant 5 V. Other minor problems were encountered with micrometre number 2, which would get stuck and needed thorough cleaning.

In addition to the Brewer MKIII, MFRSR (Harrison *et al*., 1994), Unit 901 with custom passbands for aerosols, was available at the experimentation site collecting data simultaneously over the period May 2002 to November 2006. The MFRSR unit measures the downwelling horizontal total irradiance and diffuse irradiance, from which the direct solar component is calculated, at central wavelengths of 411, 478, 555, 672, 776, 868, and 1,043 nm. The spectral bandwidths of the MFRSR detectors are narrow (nominally 10 nm) and the central wavelengths were selected to avoid radiation absorption by water vapour.

The spectral AODs from the MFRSR were obtained by subtracting molecular contributions from the total atmospheric optical depths. First the total optical depths were calculated for clear skies by the Langley method (natural logarithm of direct-normal irradiance versus air mass) using an objective algorithm (Harrison and Michalsky, 1994). Then the contributions from Rayleigh scattering, oxygen dimer $O_2$-$O_2$ absorption, and ozone absorption were subtracted to yield AODs. The Rayleigh and $O_2$-$O_2$ components scale with atmospheric pressure and were calculated from model atmospheres for the location of the MFRSR instrument (Hansen and Travis, 1974; Michalsky *et al*., 1999).

$O_2$-$O_2$ absorption is significant only in the 478 and 1,043 nm passbands and contributes an optical depth of 0.0051 and 0.0045, respectively, for the Hobart MFRSR. The ozone component was calculated by taking the mean of the time-dependent values from an ozone empirical model for the location (Van Heuklon, 1979) and an estimate derived from an iterative quadratic best-fit calculation of the measured wavelength dependence of the AODs from the MFRSR (Michalsky *et al*., 1995) for each particular Langley optical depth determination. The reason for using the mean of the two ozone derivation methods was to reduce offsets and scatter in comparisons done with satellite-derived ozone amounts. Uncertainties associated with the derivation of the optical depths are dependent upon wavelength and arise largely from deviations in the atmospheric pressure and ozone amount from what is assumed or calculated. These uncertainties are in the range of less than 0.001 to 0.004 optical depth and are discussed in detail in Michalsky *et al*., 2001.

## 2.2 | Site characteristics and data acquisition

The Brewer MKIII #179 is deployed on the roof of the Geography Building on the Sandy Bay campus of the University of Tasmania in Hobart, Australia, at latitude 42.8806°S, longitude 147.3250°E. The site is located at 47 m above sea level and approximately 0.5 km from the Derwent River estuary, in the southeastern coastal region of the island State of Tasmania. The region is subject to westerly fronts during most of the year but with frequent interruptions by high pressure systems that bring stable weather, particularly during summer and autumn (Sturman and Tapper, 2006). Precipitation and cloud cover is frequent in all months with maxima in April and October, when cut-off low pressure systems create intense periods of rain and occasional flooding. Air quality is high during most of the year, although forest fires in summer and biomass burning in winter will create periods of high contamination (Gentilli, 1972; Sturman and Tapper, 2006).

Brewer operations began on April 4, 2002, with a schedule recording DS readings at 5° zenith angle intervals throughout the day. Allowing for daily readings of the mercury and tungsten lamps, lamp ratios and zenith sky, typically there were 20 DS observations daily at the height of the summer season and around 8 in mid-winter. In February 2016, a different schedule was introduced, which increased the frequency of DS observations to approximately half-hourly, therefore providing more observations during the short winter days. Over the entire period of study, there were a total of 157,473 observations out of which 41,324 observations were considered 'cloudless skies' (see next section).

Ancillary data were available to help separate cloudy from cloudless episodes. A sky camera recorded 180° sky images at half-hourly intervals. A Solar Light UVB Biometer broadband erythemal radiometer also recorded

irradiance every minute and was available as a daily analogue trace, which was examined for irregularities and scatter as evidence of cloud cover (Gröbner and Meleti, 2004).

### 2.3 | Physical model

The technique uses DS observation in any one of the five wavelength slits ($\lambda$) used by the Brewer instrument. Neglecting sulphur dioxide and nitrogen dioxide effects, the observed direct-normal irradiance $I_\lambda$ may be written in terms of extinction by Rayleigh scattering, ozone absorption and aerosol extinction using Beer's law (Liou, 2002):

$$I_\lambda = T_{\lambda F} * r_v * I_{\lambda 0} \exp\left(-m_O \tau_{\lambda O} - m_R \tau_{\lambda R} - m_A \tau_{\lambda A}\right) \quad (1)$$

which after taking the natural logarithm, rearranging terms, and solving for $\tau_{\lambda A}$ becomes,

$$ln\left(\frac{I_\lambda}{T_{\lambda F} * r_v}\right) + m_O k_{\lambda O} O_3 + m_R \tau_{\lambda R} = ln\left(I_{\lambda 0}\right) - m_A \tau_{\lambda A} \quad (2)$$

$$ln\left(\frac{I_\lambda}{T_{\lambda F} * r_v * I_{\lambda 0}}\right) + m_O k_{\lambda O} O_3 + m_R \tau_{\lambda R} = -m_A \tau_{\lambda A} \quad (3)$$

$$\tau_{\lambda A} = -\left(1/m_A\right)\left[ln\left(\frac{I_\lambda}{T_{\lambda F} * r_v * I_{\lambda 0}}\right) + m_O k_{\lambda O} O_3 + m_R \tau_{\lambda R}\right] \quad (4)$$

where for every wavelength $\lambda$ we define $I_{\lambda 0}$ as extraterrestrial intensity, $k_\lambda$ is extinction coefficient ($cm^{-1}$), $\tau_\lambda$ is optical depth, $m$ is air mass, and subscripts $O$, $R$, and $A$ stand for ozone, Rayleigh scatter and aerosol, respectively. Finally, $O_3$ represents total column ozone in the atmosphere (cm-atm), $r_v$ is a sun-earth distance correction (Spencer, 1971), and $T_{\lambda F}$ is the filter transmission in any of the five filters that are used by the instrument.

AOD $\tau_{\lambda A}$ may be derived using Langley extrapolation if surface intensity $I_\lambda$ is measured and column ozone and Rayleigh optical depth are known. The technique consists of plotting the left-hand side of Equation 2 versus $m_A$, with the negative of the slope being $\tau_{\lambda A}$. Early studies used the technique for cloudless, stable conditions (Marenco *et al.*, 2002; Sellito *et al.*, 2006). The method is demanding in terms of constancy of ozone and AOD during the diurnal cycle (Marenco, 2007; Diemoz *et al.*, 2016). A more commonly adopted method is to solve for $\tau_{\lambda A}$ for every measurement of $I_\lambda$ in Equation 3, thus avoiding the need to specify a diurnally constant $\tau_{\lambda A}$. However, in this approach $I_{\lambda 0}$ needs to be specified, which may be obtained using absolute calibrations of the irradiance (Bais, 1997; Gröbner and Meleti, 2004; Kazadzis *et al.*, 2007) or by comparison with a travelling standard (Kumharn *et al.*, 2012).

Our approach uses the Langley method as described above to obtain a reliable $I_{\lambda 0}$, which is then used in Equation 4 to retrieve $\tau_{\lambda A}$. To ensure cloudless conditions, cloud filtering is applied using the variability in the raw signal and ozone during a DS cycle. Accurate extraterrestrial intensities ($I_{\lambda 0}$) are important in obtaining reliable AOD values. In Section 3.4, we describe how this parameter is obtained, using calibration with a travelling standard supplemented by radiometric measurements on cloudless, very transparent and stable days. Finally, AOD $\tau_{\lambda A}$ is calculated once the model has been corrected for cloudy episodes and long-term changes in $I_{\lambda 0}$.

## 3 | DATA PROCESSING AND ANALYSIS

### 3.1 | Processing of raw signals

Each of the five raw DS signals are first processed and subsequently averaged. The processing includes correcting for dark count, changes to count rate and dead time (Kipp and Zonen, 2014). Temperature corrections follow using the five temperature coefficients (one for each of the five slits) listed in the Instrument Configuration File. Correction for internal polarization effects was developed using data for field method 3 presented by Cede *et al.* (2006). Kriging interpolation provided estimates at 0.1° intervals in the 60°–80° solar zenith angle range where the effect is noticeable.

### 3.2 | Determination of Rayleigh scattering optical depths ($\tau_{\lambda R}$), ozone absorption coefficients ($k_{\lambda O}$), and air masses ($m_R, m_O, m_A$)

Calculation of the Rayleigh spectral optical depth followed the method of Bucholtz (1995), which uses an integral of volume scattering coefficient $k_{\lambda R}$ from the reference surface ($z_0$ = 47 m above sea level) to the top of the atmosphere and corrects for both temperature and pressure. The resultant spectral optical depths are then convolved with the five instrument slit functions ($S(\lambda)$) to obtain the five weighted $\tau_{\lambda R}$ values, one for each slit. An Atlas plus Modtran spectrum (Mayer *et al.*, 2011) is used, interpolated to 0.01 nm. All pressure and temperatures are referred to a mid-latitude summer atmosphere (Anderson *et al.*, 1986).

Ozone absorption coefficients are derived using the method of Bernhard *et al.* (2005) with the Bass-Paur

ozone cross-sections (Bass and Paur, 1985) and the Barnes and Mauersberger (1987) corrections. These were then convolved with the instrument slit function. As in the Rayleigh optical depth calculations, an AFGLMS atmosphere is used with an Atlas plus Modtran spectrum (Mayer *et al*., 2011) interpolated to 0.01 nm.

Air masses for Rayleigh scatter ($m_R$) were estimated following Kasten and Young (1989), allowing for station height (47 m) and surface pressure using daily measurements taken at Hobart Airport (42.836°S; 147.507°E). Air masses for ozone ($m_O$) were estimated for each observational record using the Evans and Komhyr (2008) revised formula. Air masses for aerosol ($m_A$) were estimated using Kasten's formula (Kasten, 1966), which is based on Schnaidt's proposal for water vapour (Schnaidt, 1938). This formula is suitable for aerosols since they typically reside in the boundary layer, with their vertical profile being more similar to water vapour than to other gases.

### 3.3 | Determination of the extraterrestrial intensity $I_{\lambda 0}$

Our geographic location and financial constraints prevented regular inter-comparisons with a standard instrument. On two occasions, the Brewer travelling standard #109 was used to obtain an extraterrestrial intensity calibration. The two periods were from February 21, 2016, to March 12, 2016, and from February 25, 2019, to March 1, 2019. The calibration consists of simultaneous measurements between the *travelling* standard and Hobart Brewer. AOD from the travelling standard ($\tau_{\lambda A}$) obtained via Equation 2 is substituted in the extinction calculation for the Hobart instrument in Equation 1. The required $I_{\lambda 0}$ is obtained, this term being an instrument-dependent value (Savastiouk, 2019; 2016).

Langley analyses on cloudless, transparent and very stable half-days have been performed to supplement the calibrated observations of $I_{\lambda 0}$. This type of approach has been proven useful to retrieve AOD with a Brewer spectrophotometer in the visible (Gröbner and Meleti, 2004; Diemoz *et al*., 2016) and ultraviolet ranges (Cheymol and De Backer, 2003; De Bock *et al*., 2010). We have used results from these studies to apply the following criteria:

1. A DS cycle of five measurements is accepted if the standard deviation of column ozone is less than 2.5 Dobson Units (DU). This condition successfully screens out most of the cloud-contaminated cases (Cheymol and De Backer, 2003; Gröbner and Meleti, 2004).
2. Data are accepted for the Langley analysis if the relative air mass is lower than 4 (Gröbner and Meleti, 2004). This criterion is applied to eliminate noisy data affected by large solar zenith angles (Cheymol and De Backer, 2003; Gröbner and Meleti, 2004).
3. A half-day is considered acceptable if the number of valid groups of 5 DS individual measurements is above or equal to 5 (25 individual measurements). This half-day criterion is coherent with a value of 10 DS groups (50 individual measurements) required for an entire day by other authors (Cheymol and De Backer, 2003; Diemoz *et al*., 2016).
4. A half-day is considered acceptable if the range of air masses covered by the measurements is above 1.3 (Gröbner and Meleti, 2004; Diemoz *et al*., 2016). Requiring a minimum air mass range favours the significance of the linear regression (Cheymol and De Backer, 2003; Gröbner and Meleti, 2004; Diemoz *et al*., 2016).
5. A half-day is considered acceptable if the AOD from the Langley analysis is lower than 0.17. This condition ensures very low aerosol loads, similar to the value of 0.11 used by Gröbner and Meleti (2004) for the visible range.
6. To minimize errors, only Langley plot intercepts with standard error lower than 0.04 were considered as suitable.

Because the signal is strongest and errors in ozone absorption are small (Sellito *et al*., 2006; Kumharn *et al*., 2012), the 320 nm channel is used to represent the UV region for purposes of examining the spectral optical depths across the UV and visible regions in this study.

A total of 341 half-days (approximately 20 per year) fulfilled the criteria and were selected for the Langley analyses. These were also checked by examining analogue traces from a Solar Light UVB Biometer and sky photographs when available. Having established the required pristine cloudless half-days, a plot of $ln(I_\lambda/T_{\lambda F}r_\upsilon) + m_O\tau_{\lambda O} + m_R\tau_{\lambda R}$ in the $y$ axis and $m_A$ in the $x$ axis (Equation 2) gives $ln(I_{\lambda 0})$ as an intercept at zero air mass, and hence an estimate of the extraterrestrial intensity (ETI), $I_{\lambda 0}$. Examination of the temporal trend in $\ln(I_{\lambda 0})$ in Figure 2 reveals three distinct periods: a decreasing trend from start of operations to approximately the end of March 2006; a constant trend from April 2006 to the end of February 2016; and a different constant trend until the end of the study period. On February 26, 2016 the photomultiplier voltage was increased (Savastiouk, 2016) which increased $\ln(I_{\lambda 0})$. Variability in $I_{\lambda 0}$ is due to both changes in sensitivity and day- to - day measurement uncertainties. To account for this change in $\ln(I_{\lambda 0})$ over the entire study period, we applied linear regression fittings to each temporally distinct period, obtaining slopes

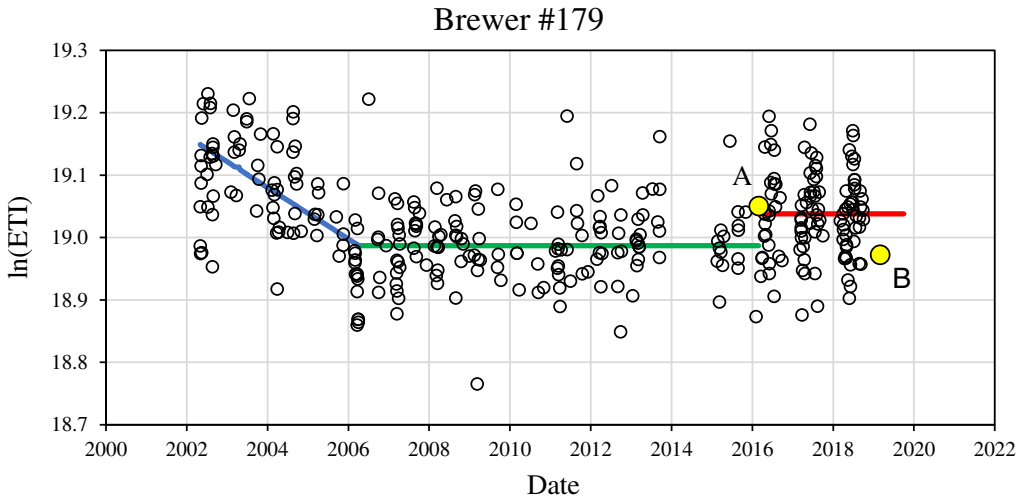


**FIGURE 2** Plot of ln(ET I) versus date for Brewer #179. Blue line: Linear trend given by ln(ET I) = 19.140 (±0.013) − 1.3E -4 (±1.6E−5) * (day number from May 1, 2002). Green line: Constant = 18.992 (±0.0 6). Red line: Constant = 19.037 (±0.06). Yellow dots denote calibration by travelling standard #109: (a) 19.0505 (±0.03) on February 26, 2016, (b) 18.9725 (±0.03) on February 27, 2019

and corresponding standard errors of $(-0.0414 \pm 0.0066)$ per year, $(0.0006 \pm 0.0019)$ per year, and $(0.0005 \pm 0.0078)$ per year, respectively, for the 320 nm channel. Whilst the first period exhibits a decreasing trend, the second and third periods have non-significant trends and the $\ln(I_{\lambda 0})$ can be considered constant with values of 18.992 and 19.037, respectively, with a standard deviation of 0.06. The standard deviation of our estimates of $\ln(I_{\lambda 0})$ is a likely estimate of the accuracy of our extrapolation technique.

For comparison purposes, $\ln(I_{\lambda 0})$ is plotted in Figure 2 for the two data points (yellow) obtained by calibration with the travelling standard. The mean figure obtained for the third period is in approximate agreement with the travelling standard estimate of $19.050 \pm 0.03$ obtained from February 22, 2016, to March 1, 2016. The second travelling standard calibration was obtained from February 25, 2019, to March 1, 2019 (which was outside the study period). Although results for the second calibration show a small but noticeable decrease in $\ln(I\lambda 0)$ compared to the first calibration, this decrease is not detected by our Langley analyses. In the absence of simultaneous calibration standard data, and given the scatter in our extrapolation technique, we have averaged $\ln(I_{\lambda 0})$ for the last period, obtaining a figure of 19.037.

Knowing $\ln(I_{\lambda 0})$ for every day of the study period, AOD is obtained during normal operations following the method of Cheymol and De Backer (2003), and De Bock *et al.* (2010). Equation 4 is solved for $\tau_{\lambda A}$ during any time of day over a range of zenith angles under cloudless conditions. The data set allows us to study the diurnal behaviour of $\tau_{\lambda A}$ and its relationship to a range of environmental variables.

## 3.4 | Selection of cloudless cases

Filtering for cloud data is similar to that described in the above section concerning determination of the extraterrestrial intensity for cloudless half-days. First, examining analogue traces of UVB irradiance from the UVB Biometer revealed that most cloudy episodes were eliminated by requiring the standard deviation of column ozone for an individual DS cycle to be less than 2.5 DU (Cheymol and De Backer, 2003; Gröbner and Meleti, 2004). In addition, the standard deviation of $\tau_{\lambda A}$ taken from individual measurements of a DS cycle should be less than 0.02 (Gröbner and Meleti, 2004). Signals less than 10 times the dark count values have been eliminated as they indicate low light conditions and/or heavy cloud cover (Diemoz *et al.*, 2016). Finally, only $\tau_{\lambda A}$ values lower than 1 were allowed.

## 3.5 | Uncertainty analysis

A number of studies have examined uncertainties associated with the various components involved in the calculation of $\tau_{\lambda A}$, which follows from Equation 4 in the absence of clouds. Carlund *et al.* (2017) examine typical errors associated with a precision four-channel radiometer operating in the UV bands. Arola and Koskela (2004) provide typical uncertainties related to stray light, variability of aerosol load, and $NO_2$ influences in urban areas. Uncertainties of 2.1% prevail in the use of the Bass-Paur ozone cross-sections and 1% in total ozone content, arising mainly from changes in effective ozone temperature (Cheymol and De Backer, 2003).

There are also apparent changes in ozone optical depth as a result of an effective shift in wavelengths as total column ozone increases. Carlund *et al.* (2017) provides correction factors for ozone optical depth obtained for their four-channel precision UV radiometer, which range from 1.012 for 305 nm to 1.000 at 332 nm. We use only the 320 nm band in our analysis and we use no added correction for this effect.

Uncertainties in filter transmission were determined by comparing factory estimates with 1 year of average transmission estimates (November 14, 2016, to November 14, 2017) using the FW2 routine. Changes in the five filters ranged from 1.1% to −0.59% in transmission for the 14 years considered (ND0.44 = 0.785%; ND1.02 = 1.12%; ND1.40 = 0.84%; ND2.14 = −0.59%; ND2.63 = −0.24%). We have assigned an uncertainty of 1% to all filters in the analysis.

Added uncertainties relate to the extraterrestrial intensity $I_{\lambda 0}$ (Equation 1), which has been estimated in this study as 6% ($1\sigma$) for the 320 nm band. The uncertainty is twice the $1\sigma$ uncertainty in travelling standard #109 (3%), which was used to calibrate the Hobart Brewer in February 2016 (Savastiouk, 2016). Additionally, surface pressure changes of 1 hPa, if uncorrected, will also induce typical errors of around 1% in Rayleigh optical depth (Carlund *et al.*, 2003; 2017).

Finally it should be stated that there could be added uncertainties from cloud events in the records that are not eliminated by the filters and are not taken into account in this analysis. We expect that visual observation of the Langley plots would detect such events since cloud-induced radiation changes are usually large and significant. However, it is possible that subvisual cirrus or altostratus clouds might escape the filtering routines. Further studies are warranted to examine this source of uncertainty in greater detail.

All the above individual uncertainties will contribute to the magnitude of the overall uncertainty in $\tau_{\lambda A}$ as determined from Equation 4. A Monte Carlo analysis was developed to group these individual uncertainties into an overall uncertainty for $\tau_{\lambda A}$. Ten data sets covering a span in $\tau_{\lambda A}$(320 nm) from 0.114 (October 7, 2002, at 1023 AEST (UTC+10)) to 0.516 (December 20, 2015, at 1027 AEST), as listed in Table 1, are used in Equation 4, with various terms in the right-hand side of the equation being characterized by an uncertainty. For each variable $Y_i$ with a standard deviation $\sigma_{Yij}$, a random number generator produces values between 0 and 1, which feeds into a cumulative error distribution function resulting in a new value of $Y_i$. Each iteration $j$ produces new values for variables $Y_1$, $Y_2$, $Y_3$, ..., labelled $Y_{1j}$, $Y_{2j}$, $Y_{3j}$, .... These are then substituted in Equation 4 to arrive at a new estimate of $\tau_{\lambda A}$. Table 2 shows the errors in percentages used in the analysis, which are multiplied by $Y_i$ to get the standard deviation ($\sigma$). A new value of AOD from Equation 4 is estimated for each iteration using:

$$\tau_{\lambda A} = \frac{-1}{m_A}\left[\ln\left(\frac{I_\lambda}{\{T_{\lambda F}\} * r_v * \{I_{\lambda 0}\}}\right) + m_0\{k_{\lambda O}\}\{O_3\} + m_R\{\tau_{\lambda R}\}\right] \quad (5)$$

where the curly brackets denote a change from the original value, $\{Y\} = Y_0 + \delta Y$. A random number was generated $10^3$ times for each of the 10 episodes, which resulted in $10^4$ different values of $\tau_{\lambda A}$. We have assumed that terms not having curly brackets have negligible uncertainties compared to the terms considered. Appendix provides details of the technique used.

Table 3 and Figure 3 show the results of the analysis. Standard deviations ($1\sigma$ uncertainty for a normal distribution) occupy a range between 0.021 and 0.047, with an average of 0.034. There is considerable variability in the

**TABLE 1** Input data used in the uncertainty analysis

| Time (AEST) | Day | Month | Year | Col $O_3$ (D.U.) | Zenith angle (°) | $m_A$ | $\tau_{320A}$ |
|---|---|---|---|---|---|---|---|
| 1023 | 7 | 10 | 2002 | 315.1 | 70.09 | 2.931 | 0.114 |
| 1717 | 26 | 1 | 2005 | 264.6 | 65.35 | 2.395 | 0.166 |
| 0822 | 14 | 12 | 2007 | 296.6 | 49.65 | 1.544 | 0.193 |
| 0819 | 17 | 1 | 2008 | 287.2 | 54.64 | 1.727 | 0.366 |
| 1029 | 28 | 1 | 2008 | 256.3 | 34.37 | 1.211 | 0.244 |
| 1644 | 2 | 2 | 2010 | 277.7 | 60.39 | 2.022 | 0.282 |
| 1332 | 7 | 5 | 2013 | 270.5 | 62.82 | 2.187 | 0.252 |
| 1027 | 20 | 12 | 2015 | 283.4 | 28.54 | 1.138 | 0.516 |
| 1424 | 26 | 10 | 2016 | 332.0 | 44.17 | 1.394 | 0.192 |
| 1418 | 31 | 1 | 2017 | 273.8 | 35.08 | 1.222 | 0.168 |

**TABLE 2** Uncertainty in coefficients used in determination of aerosol optical depth

| Wavelength (nm) | $T_F$ (%) | $O_3$ (%) | $k_{O_3}$ (%) | $I_0$ (%) | $k_R$ (%) |
|---|---|---|---|---|---|
| 320 | 1.0 | 1.0 | 2.1 | 6.0 | 1.0 |

**TABLE 3** Standard deviation of aerosol optical depth $\tau_{320A}$ from Monte Carlo analysis

| Air mass $m_A$ | Avg. std. dev. $\tau_{320A}$ |
|---|---|
| 2.931 | ±0.021 |
| 2.395 | ±0.024 |
| 2.187 | ±0.025 |
| 2.022 | ±0.027 |
| 1.727 | ±0.031 |
| 1.544 | ±0.035 |
| 1.394 | ±0.038 |
| 1.222 | ±0.044 |
| 1.211 | ±0.044 |
| 1.138 | ±0.047 |

*Note*: A total of 10 cases were examined covering a range of aerosol optical depths. Each case was iterated 1,000 times to arrive at a standard deviation of $\tau_{\lambda A}$.

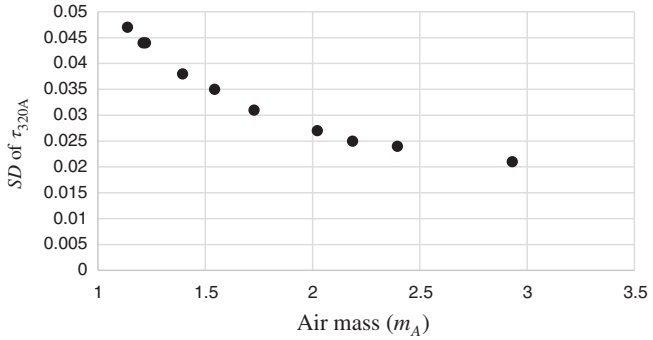


**FIGURE 3** Standard deviation of $\tau_{320A}$ versus aerosol air mass $m_A$ from the Monte Carlo analysis. A total of 10 cases were examined covering a range of aerosol optical depths. Each case was iterated 1,000 times to arrive at a standard deviation for $\tau_{320A}$

standard deviations for the 10 episodes that were executed. There is a negative dependence on air mass, which is to be expected from the equation for $\tau_{\lambda A}$. The range in standard deviations reflects the different episodes that were selected and the large number of executions in the random sampling routine. The average standard deviation of 0.034 at 320 nm is low enough to give some confidence in the ability to discriminate $\tau_{\lambda A}$ at low optical depths.

## 4 | RESULTS

### 4.1 | Seasonal variability

A histogram of the 41,324 $\tau_{320A}$ points acquired using the criteria given in Section 3 is shown in Figure 4. A frequency interval between 0.10 and 0.15 is the most common, with 47% of all episodes falling in this category. However, there is a significant tail extending to higher $\tau_{320A}$ values: there are 471 episodes with $\tau_{320A}$ in the interval 0.35 to 0.40 (1.14% frequency) and 13 episodes in the interval 0.95 to 1.0 (0.03% frequency).

Figure 5 plots monthly averages of AOD at 320 nm, along with the 5 and 95 percentiles of AOD. Table 4 provides more detailed statistics. Monthly averages feature maxima in summer months, slightly under 0.15 but decreasing towards a minimum in winter of 0.09. Very little variability is exhibited in the monthly 5 percentile values, which is approximately constant at 0.05. By contrast, the 95 percentile values show high variability throughout the year with a maximum in January of 0.39 and decreasing to 0.16 in July. This pattern is typical of an environment with low aerosol load but with occasional intrusions of heavily contaminated air masses mostly related to bushfire events (Clark, 2020).

### 4.2 | Diurnal variability

All hourly data were pooled together according to month and Australian Eastern Standard Time (AEST) hours. This resulted in a matrix of 12 months by 24 hr. Each of the 41,324 $\tau_{320A}$ data points in the study falls into one of the bins. $\tau_{320A}$ for each month and each hour was normalized by subtraction of its noon-time $\tau_{320A}$ corresponding to that month. All normalized monthly and hourly $\tau_{320A}$ were then averaged over the year to obtain the diurnal change in AOD shown in Figure 6 (orange line). A pattern of increasing $\tau_{320A}$ towards noon is seen, with a slight decrease in the afternoon. The normalization procedure that was used masks a marked seasonality in average noon-time $\tau_{320A}$ values, from 0.167 in January to 0.088 in July. Despite the diurnal pattern, it must be emphasized that each individual monthly $\tau_{320A}$ has a large standard deviation of ±0.09.

### 4.3 | Transient events

Seasonal changes in $\tau_{320A}$ vary with the intensity of solar radiation, which influences photochemical processes in

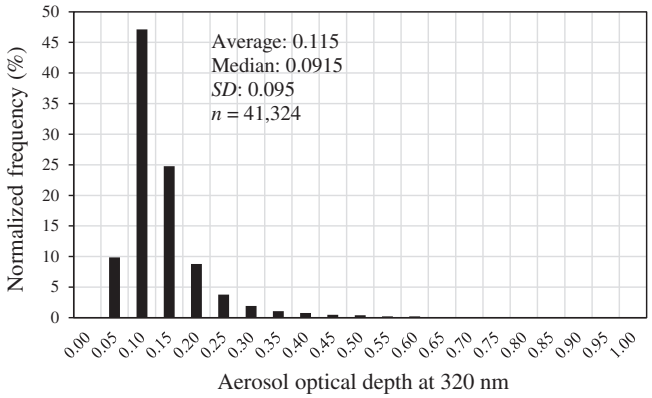


FIGURE 4 Normalized histogram of aerosol optical depth at 320 nm for Hobart station (2002–2018)

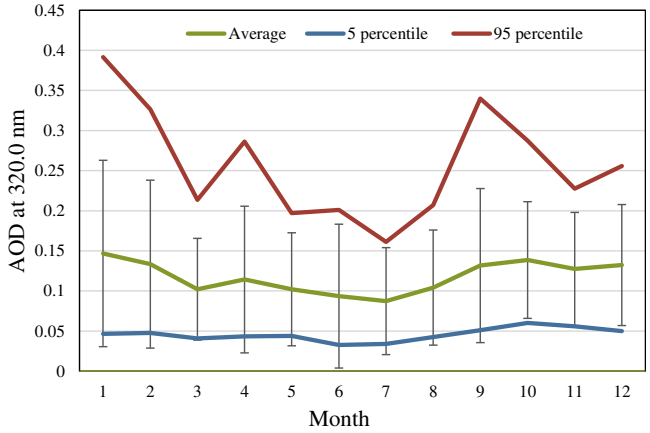


FIGURE 5 Statistics for monthly AOD at 320 nm [Colour figure can be viewed at wileyonlinelibrary.com]

the atmosphere and behaviour of the surface boundary layer. To examine these processes further, wind rose diagrams with 16 cardinal directions are shown for each month in Figure 7. A colour scheme also shows the AOD characteristics associated with each of the wind directions. During summer months, the flow is essentially southeast to northwest following the orientation of the Derwent Valley. Sea breezes from the southeast are typical in summer months and are characterized by $\tau_{320A}$ in the range of 0.1 to 0.2. By contrast, very low $\tau_{320A}$ between 0 and 0.1 is associated with down-valley flows from the northwest during the winter months from May to August.

Large $\tau_{320A}$ exceeding 0.3 is not frequent (Figure 4) and is likely to be caused by local sources, related for example to controlled or accidental burning of forests, stagnation/sea breeze re-circulation events, and in winter, smoke from domestic heating using wood stoves (Lyons and Cole, 1976; Janjai *et al.*, 2009; Borchers-Arriagada *et al.*, 2019).

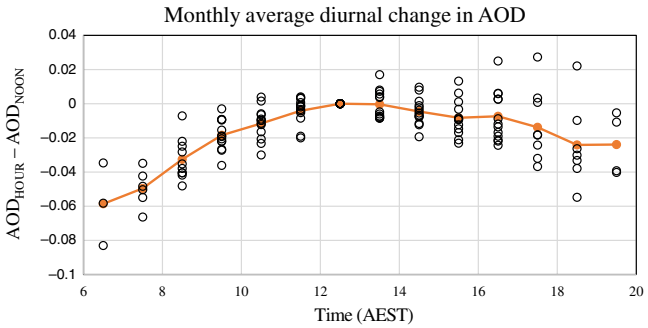


FIGURE 6 Diurnal change in AOD at 320 nm. All AOD data have been averaged by month and daylight hour. Each point is the mean of the noon-normalized monthly and hourly AOD averaged over all years (one point for each month in the hour bin). The orange line is the average of the hourly means and has an average standard deviation of 0.021. The standard deviation of the individual hourly mean points representing each month is 0.09 [Colour figure can be viewed at wileyonlinelibrary.com]

## 4.4 | Inter-annual trends

The Brewer MKIII at the Hobart station became operational in April 2002 and the system has remained functional until the present. A new computer was installed at the end of 2014, and in the change-over the DS files for 2014 were lost, so no AOD data for 2014 were available. Apart from this period, continuous $\tau_{320A}$ has been acquired and is available for analysis. Figure 8 plots yearly averages for years with complete records from 2003 to 2018 inclusive. Despite the large standard deviations, the slope statistic shows an increasing trend with a probability less than 1% that it occurred by chance. The continuous pattern is likely a result of the increasing incidence of large bushfires in the Australian region, including their size and duration (Clark, 2020), which is partly a result of increasing fire-prone weather events (Fox-Hughes *et al.*, 2014; Dowdy, 2018). Figure 9a shows yearly precipitation from 2002 to 2019 plotted as anomalies from their 30-year means (1991–2020). Only four out of the 18 years show positive anomalies and 2006 reached the lowest value on record with a precipitation anomaly of −193.5 mm.

Maxima in the yearly averages are reached in 2015 with a value of $\tau_{320A} = 0.151$. This particular year was characterized by the driest spring on record (Figure 9b) induced by strong El Niño and Southern Ocean Dipole weather events (TFS, 2016). In October, Tasmania experienced a range of regional fires across the southeastern sector of the State near Hobart. Weekly averages of $\tau_{320A}$ during 2015 at the Hobart station are shown in Figure 10 along with long-term weekly averages for the period 2003–2018 (excepting 2014 due to the missing data).

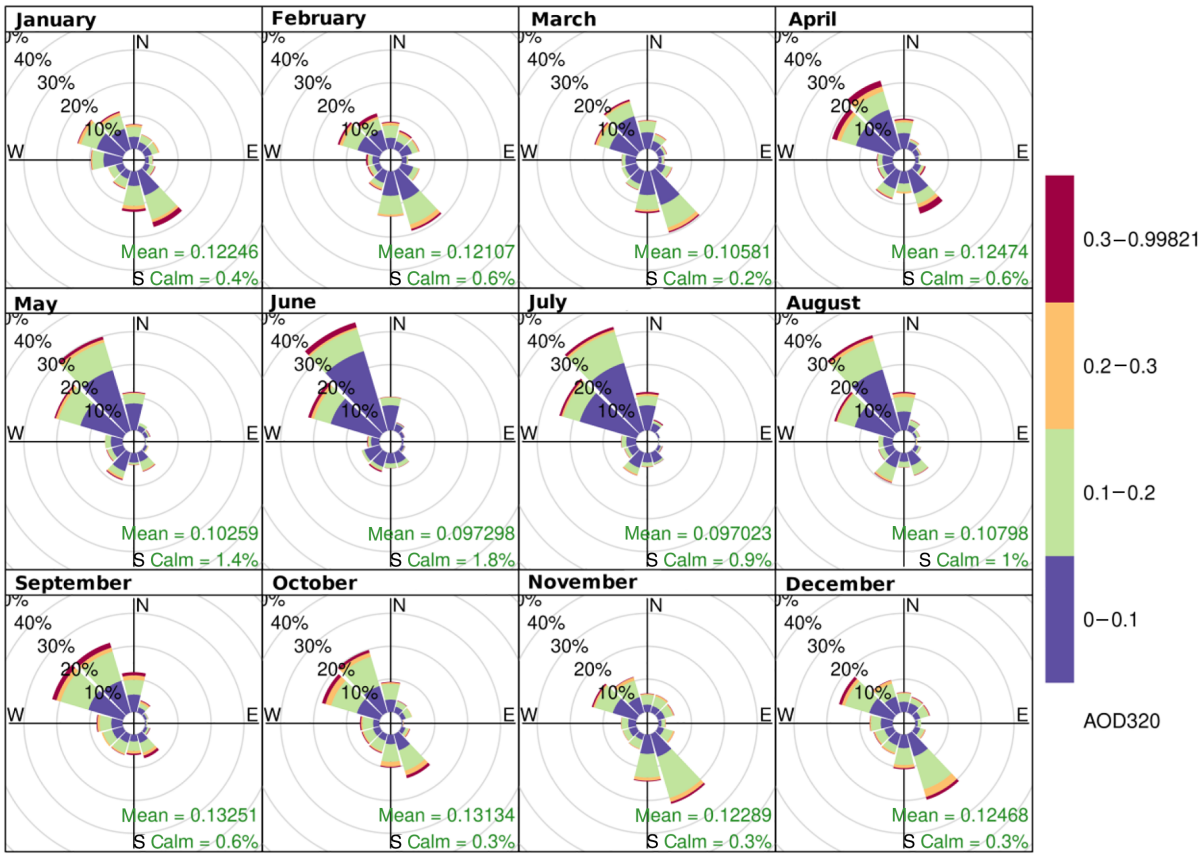


**FIGURE 7** Wind rose diagrams for the Hobart Brewer station. Colours denote the range in AOD magnitude for a given direction and frequency

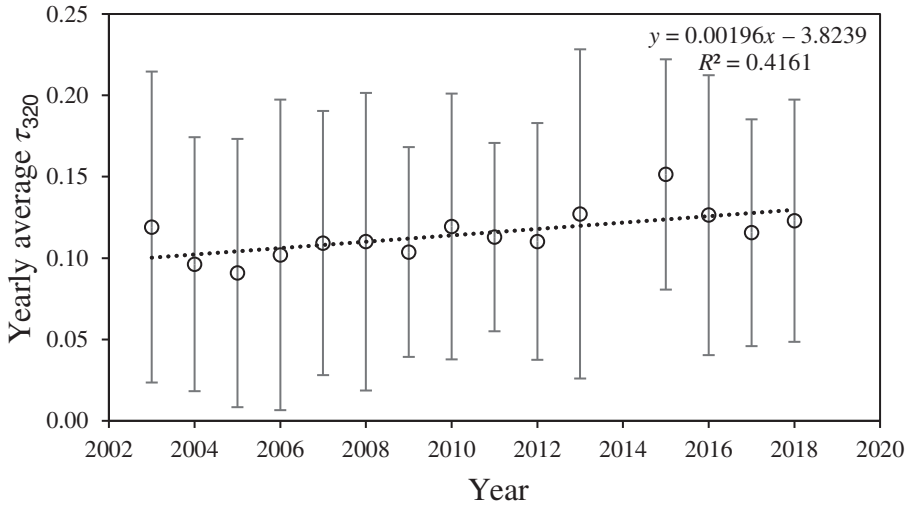


**FIGURE 8** Yearly statistics for aerosol optical depth at 320 nm ($\tau_{320A}$). The slope is significant at the 99% level of confidence. Data for 2015 encompass a large fire event in the vicinity of the Hobart station in the second half of 2015. A pronounced seasonal signal affects the magnitude of the standard deviation

Long-term averages clearly show a seasonal signal, with maxima of around 0.15 in early January and decreasing to around 0.07 during winter mid-year. AOD records for the first half of 2015 fall mostly within 1 standard deviation of the long-term record. However, in the second half of 2015 the $\tau_{320A}$ increase above the long-term value, reaching a maximum 0.370 in Week 40, which is in the first half of October. These high $\tau_{320A}$ events are rare in Tasmania and correspond to extinction of UV radiation by aerosols created by biomass burning. However, only 2% of all $\tau_{320A}$ recorded have values above 0.35 (Figure 4).

## 4.5 | Wavelength dependence

The availability of the Brewer and MFRSR data sets allowed us to examine if the Ångström relationship

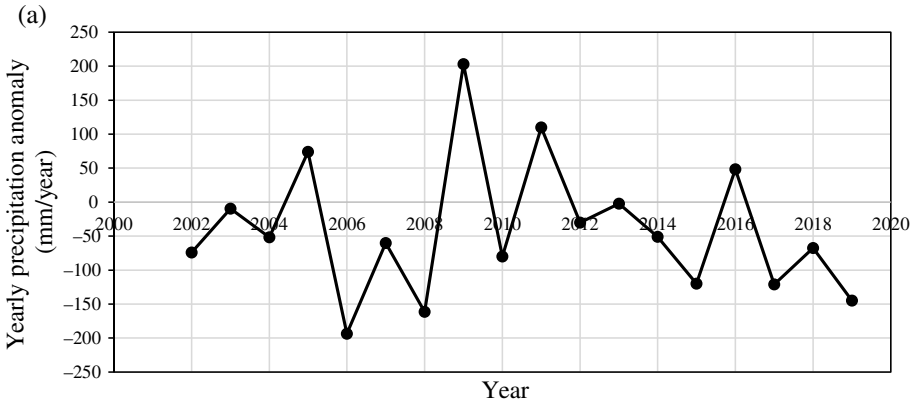


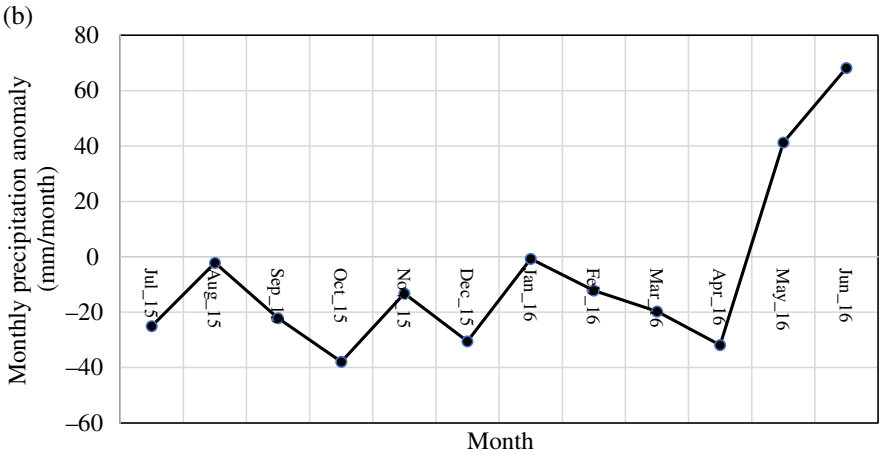


**FIGURE 9** Precipitation anomalies for Hobart Airport (42.836°S, 147.507°E). (a) Yearly anomalies from 2002 to 2019. b) Monthly anomalies for the year 2015/2016 [Colour figure can be viewed at wileyonlinelibrary.com]

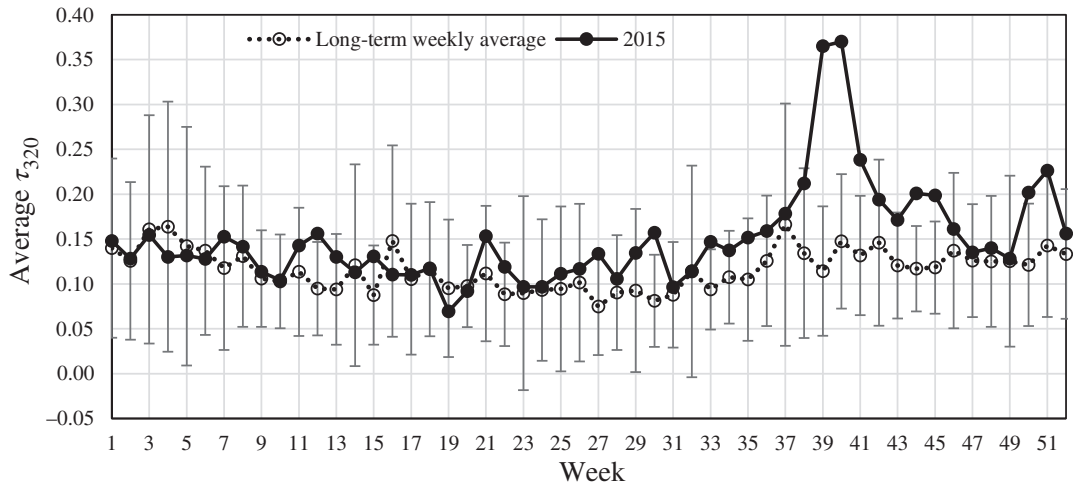


**FIGURE 10** Weekly averages of AOD at 320 nm for the Hobart Brewer station. White circles: Weekly long-term averages for $\tau_{320A}$ over the years 2003 to 2018, discounting missing data in 2014. Also shown are the 1$\sigma$ standard deviations. Black circles: Weekly averages for 2015

(Ångström, 1929) in the visible range can also be applied to the UV range. Using the Ångström analysis, a spectral optical depth $\tau_{\lambda A}$ can be described as a function of wavelength given in microns by convention:

$$\tau_{\lambda A} = \beta \lambda^{-\alpha} \quad (6)$$

where the parameters $\beta$ and $\alpha$ relate to the total extinction and aerosol size, respectively (Michalsky *et al.*, 2001; Janjai *et al.*, 2009; Kumharn *et al.*, 2012). Our study examines values of α in a variety of air mass conditions.

It is possible to compare AOD at 320 nm with visible bands from the MFRSR. The procedure followed was to

select periods between 2002 and 2006 with simultaneous Brewer and MFRSR data. AOD is provided by MFRSR data over a half-day period using the Langley method as discussed previously. For comparison purposes the Brewer data is then averaged over the corresponding half-day. The last MFRSR band at 1043 nm gives results very similar to the 868 nm band. For data processing purposes, the 1,043 nm band has been dropped and replaced by the Brewer UV band operating at 320 nm. Thus, in the Ångström analysis for this study, AOD data from seven wavelengths are used, one from the Brewer (320 nm) and six from the MFRSR (411, 478, 555, 672, 776 and 868 nm).

The natural logarithm of the Ångström relationship is:

$$\ln(\tau_{\lambda A}) = -\alpha \ln(\lambda) + \ln(\beta) \tag{7}$$

and the Ångström exponent $\alpha$ is obtained as the negative slope of the $\ln(\tau_{\lambda A})$ versus $\ln(\lambda)$ plot using least square statistics. In some studies, variability of $\alpha$ with wavelength is derived using increments of $\ln(\tau_{\lambda A})$ and $\ln(\lambda)$ (Eck *et al*., 1999; Kaskaoutis *et al*., 2006):

$$\alpha = -\frac{d\ln(\tau_{\lambda A})}{d\ln(\lambda)} = -\frac{\ln\frac{\tau_{\lambda 2}}{\tau_{\lambda 1}}}{\ln\frac{\lambda_2}{\lambda_1}} \tag{8}$$

A number of studies (Soni *et al*., 2011; Kedia and Ramachandran, 2009; Kaskaoutis et al., 2007; 2006; Schuster *et al*., 2006; Eck *et al*., 2003; 1999; Reid *et al*., 1999) document that $\alpha$ is not constant with wavelength but is best described by a second order polynomial relationship between $\ln(\tau_{\lambda A})$ and $\ln(\lambda)$:

$$\ln(\tau_{\lambda A}) = C_0 + C_1 \ln(\lambda) + C_2 \ln^2(\lambda) \tag{9}$$

The sign of $C_2$ is related to the curvature of $\ln(\tau_{\lambda A})$ versus $\ln(\lambda)$, where $C_2$ may be given explicitly as:

$$C_2 = \frac{1}{2}\frac{\partial^2 \ln(\tau_{\lambda A})}{\partial \ln(\lambda)} = -\frac{1}{2}\frac{\partial \alpha}{\partial \ln(\lambda)} \tag{10}$$

$$\alpha = -\frac{\partial \ln(\tau_{\lambda A})}{\partial \ln(\lambda)} = -C_1 - 2C_2 \ln(\lambda) \approx C_2 - C_1 \tag{11}$$

Biomass burning environments are characterized by fine aerosols in accumulation mode with positive curvature in $\alpha$ (or negative $C_2$ in Equation 10) as measured by Eck *et al*. (2003; 1999) in Bolivia and Zambia, Kumar *et al*. (2013) in South Africa, and Reid *et al*. (1999) in Brazil, amongst others. Measurements in urban environments and polluted regions also exhibit positive $\alpha$ curvature (Soni *et al*., 2011; Kaskaoutis et al., 2007; Kedia and Ramachandran, 2009). Cleaner non-contaminated environments including oceanic regions and deserts have a strong component of coarse mode aerosols with negative $\alpha$ curvature, as evidenced in measurements taken over the Arabian sea (Kedia and Ramachandran, 2009), at Nauru Island in the western Pacific (Kaskaoutis et al., 2007), and over deserts (Kaskaoutis et al., 2007; Kedia and Ramachandran, 2009; Eck *et al*., 1999).

Theoretical studies use Mie radiation theory on known aerosol size distributions, and these confirm features of the $\alpha$ curvature (Eck *et al*., 1999; Schuster *et al*., 2006). Schuster *et al*. (2006) used bi-modal aerosol size distributions with varying fine to total particle concentrations to show that $\alpha$ is a strong function of effective radius when distributions are dominated by fine particles. Alternatively, the variability of $\alpha$ with effective radius is essentially flat when the distribution is dominated by coarse particles.

In our analysis, we apply Equations 7 to 11 to aerosol characteristics for our study area. However, merging two different data sets is difficult due to temporal variability in each data set within the half-day averages. To minimize uncertainties, episodes with half-day Brewer observations less than two were eliminated. Application of this criterion left 89 episodes available for analysis.

To investigate the character of the $\tau_{\lambda A}$ wavelength dependence, three episodes were selected which exhibited different curvature. These are shown in Figure 11. At low 555 nm optical depth, the curvature is concave and $C_2$ is positive. Increasing optical depths will result in no curvature and then convex, negative $C_2$ curvature at high optical depths. To characterize the relationship further, the curvature coefficient $C_2$ was extracted from all 89 half-day episodes (Figure 12). There is an inverse relationship between AOD at 555 nm and $C_2$ curvature. The linear regression in Figure 12 is significant at the 95% confidence level.

Using the approximation of Equation 11 (Kaskaoutis *et al*., 2007; 2006 Schuster *et al*., 2006), a frequency plot of $C_2 - C_1$ ($\approx\alpha$) is estimated for all episodes and is shown in Figure 13. Low, positive values dominate, with a median $\alpha$ value of 0.605. These results indicate the dominance of coarse mode aerosols, which would be expected in a marine environment with relatively low contamination (Holben *et al*., 2001).

## 5 | DISCUSSION AND CONCLUSION

This study has developed an AOD climatology for Hobart, Australia, based on DS measurements from a

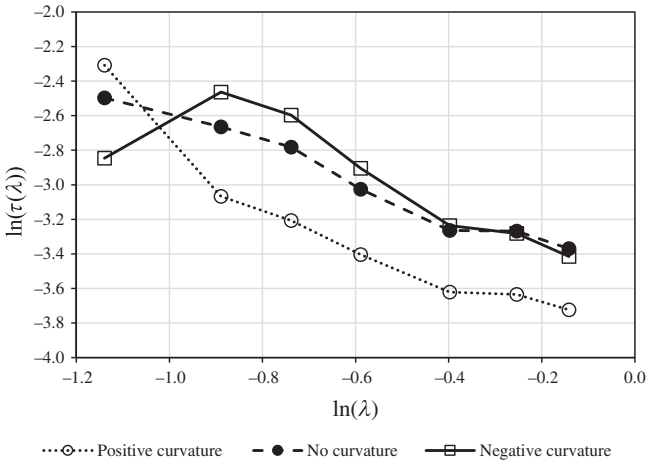


**FIGURE 11** Plot of ln($\lambda$) versus ln($\tau$ ($\lambda$)) for three half-days exhibiting positive curvature (February 2, 2003), no curvature (November 29, 2003) and negative curvature (August 17, 2004). Second order polynomial fit s are: Positive curvature: ln($\tau$ ($\lambda$)) = −3.6349 + 0.5358 * ln($\lambda$) + 1.4590 * ln 2($\lambda$); $R^2$ = 0.98 no curvature: ln($\tau$ ($\lambda$)) = −3.5217 − 0.8712 * ln($\lambda$) + 0.0513*ln 2($\lambda$); $R^2$ = 0.97 negative curvature: ln($\tau$ ($\lambda$)) = −3.8678 − 2.6627 * ln ($\lambda$) − 1.4632 * ln 2($\lambda$); $R^2$ = 0.85

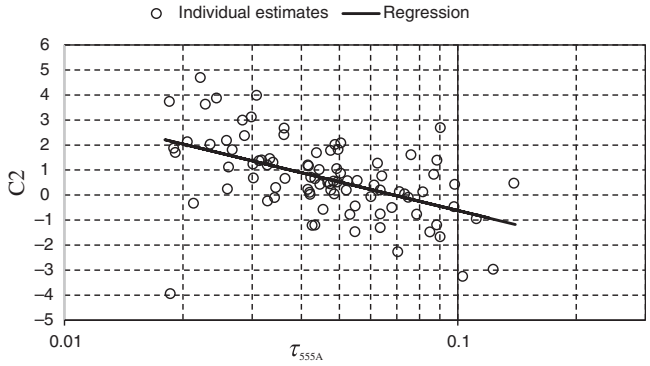


**FIGURE 12** Plot of $\tau_{555A}$ versus curvature coefficient $C_2$ for all 89 half-day episodes. A linear regression fit gives $C_2$ = −1.6517 ln($\tau_{555A}$) − 4.4235; $R^2$ = 0.255

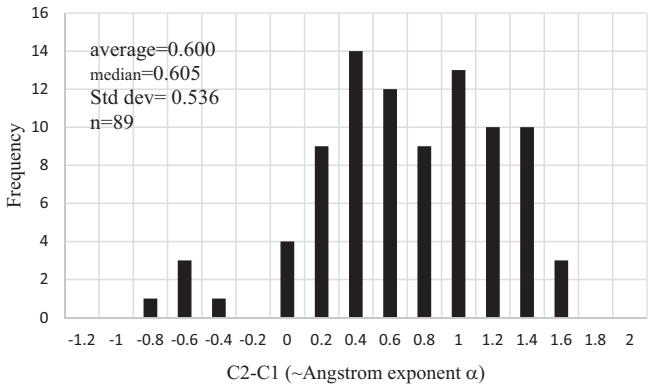


**FIGURE 13** Frequency plot of C2-C1 for all data. [Correction added on 18 August 2022, after first online publication: This is an updated version of Figure 13]

Brewer MKIII. The technique uses Beer's law to solve for AOD at 320 nm. The study requires accurate extraterrestrial irradiance $I_{\lambda 0}$ (ETI), which was not readily available due to infrequent calibration with a travelling standard. The calibrated ETI's were supplemented by applying Beer's law to a total of 341 cloudless half-days throughout the study period. The resultant pattern shows an initial linear decrease in ln(ETI) until January 2006, followed by a period where ln(ETI) is constant, and a third period after February 2016 where ln(ETI) is slightly higher but constant. There is large scatter in the ln(ETI) that results in an uncertainty that is twice as large as the ETI uncertainty of the travelling calibration standard.

The analysis next extracts cloudless days and matches each episode with a corresponding ozone column and ln(ETI), this last value being obtained by interpolation of the trends discussed above. Equation 4 is then solved for $\tau_{320A}$ as this variable is the only unknown (Cheymol and de Backer, 2003; De Bock *et al.*, 2010). An overall uncertainty for $\tau_{\lambda A}$ is obtained by using a stochastic technique employing a range of input conditions with their individual uncertainties. Results presented in Table 3 show 1$\sigma$ uncertainties ranging from ±0.021 to ±0.047 and averaging ±0.034. These figures are larger than the 2$\sigma$ uncertainty of between ±0.02 and ±0.04 reported by Lopez-Solano *et al.* (2018) for the 320 nm wavelength. These differences are likely to be a result of the larger ETI uncertainty in this study.

Our monthly climatology shows a distinct seasonality (Figure 5 and Table 4) with highest values in summer (January average 0.147 ± 0.116) and lowest in winter (July average 0.087 ± 0.066). Our seasonal trends agree with measurements at other locations employing a variety of methods and instruments, for example, using Brewer spectrometers (Kerr, 2002; Cheymol and De Backer, 2003; Kazadzis *et al.*, 2007), other UV spectrometers (Wenny *et al.*, 2001; Cachorro *et al.*, 2002), and satellite models (De Bock *et al.*, 2010). This is likely to be a result of increased photochemical activity with higher solar radiation as well as greater instability in the summer atmosphere leading to increased suspension of aerosols. Along with increased average AOD in summer, the range of optical depths experienced in summer is also higher.

The city of Hobart is located in the Derwent Valley and as a result its climate is strongly influenced by the northwest-southeast valley orientation (Gentilli, 1972; Sturman and Tapper, 2006). In winter, the region is under the influence of a stable air mass from the central highlands bringing light northwest winds and relatively low levels of contamination (see June, July and August in Figure 7). Two processes occur as the seasons change towards summer: first, the winter inversion is broken

**TABLE 4** Monthly statistics for aerosol optical depth ($\tau_{320A}$) obtained at the Hobart Brewer site

| | 1% | 25% | 50% | 75% | 99% | Std. dev. | Number |
|---|---|---|---|---|---|---|---|
| January | 0.020 | 0.083 | 0.116 | 0.163 | 0.665 | 0.116 | 5207 |
| February | 0.024 | 0.081 | 0.105 | 0.140 | 0.625 | 0.106 | 2950 |
| March | 0.027 | 0.065 | 0.086 | 0.120 | 0.347 | 0.063 | 3132 |
| April | 0.031 | 0.065 | 0.087 | 0.125 | 0.527 | 0.091 | 2972 |
| May | 0.029 | 0.066 | 0.087 | 0.118 | 0.377 | 0.070 | 2358 |
| June | 0.010 | 0.055 | 0.074 | 0.099 | 0.541 | 0.089 | 2719 |
| July | 0.019 | 0.058 | 0.074 | 0.097 | 0.449 | 0.066 | 2920 |
| August | 0.023 | 0.069 | 0.086 | 0.118 | 0.366 | 0.072 | 2937 |
| September | 0.031 | 0.082 | 0.104 | 0.140 | 0.494 | 0.096 | 3105 |
| October | 0.042 | 0.097 | 0.121 | 0.157 | 0.401 | 0.072 | 3869 |
| November | 0.033 | 0.090 | 0.114 | 0.149 | 0.393 | 0.071 | 4308 |
| December | 0.031 | 0.087 | 0.121 | 0.156 | 0.415 | 0.075 | 4299 |

*Note*: Data covered the period from May 1, 2002, to October 24, 2017.

leading to increased wind speed, solar radiation and convection; and second, sea breezes from the southeast are increasingly active (see September, October and November in Figure 7). It is interesting to note that sea breeze events are not characterized by very low 320 nm AOD's but occupy a dominant range between 0.1 and 0.2. This is typical of oceanic areas, although most reported data for these regions have been obtained in the visible bands (Torres *et al.*, 2002; Kaskaoutis *et al.*, 2007).

West and northwest winds occur all year and in spring/summer northwest winds are related to bushfire events or controlled burning that usually occurs in spring before the summer fire season. In southeastern Tasmania, fire-prone weather is characterized by downward transport of very dry air having high momentum due to topographic effects related to passage of cold fronts or upper tropospheric throughs (Fox-Hughes *et al.*, 2014; Fox-Hughes, 2015). In Figure 7, these events are typically connected to 320 nm AOD's above 0.3. Recirculation of contaminants is also a feature of sea breezes, which could explain the high AOD levels associated with southeast winds. Models predict increased frequency of fire-prone weather in southeastern Tasmania during spring (Fox-Hughes *et al.*, 2014), which is in agreement with our interannual increases in 320 nm AOD (Figure 8).

Availability of visible spectrum AOD's from MFRSR data was available for the Hobart site, allowing us to examine spectral changes in AOD's. Concurrent data with the Brewer were only available from May 2002 to November 2006, and in the case of the MFRSR only as half-day averages. Spectral AODs from the two data sets were compared after ensuring both data sets had low variability in their half-days. Results confirm that the two data sets are coherent, and that the Ångström exponent varies with wavelength and is dependent on aerosol type (Schuster *et al.*, 2006; Kaskaoutis *et al.*, 2007). An average Ångström exponent value of 0.600 ± 0.536 standard deviation was obtained, typical of oceanic-type air masses possessing coarse-mode aerosols with a positive wavelength dependence curvature in AOD. High AOD events have also been sampled and these are likely related to occasional biomass burning in the surrounding environment. We have measured an increase in yearly average $\tau_{320A}$ of 0.002 ± 0.0006.

In conclusion, our study has shown that the Hobart Brewer site exhibits low values of AOD in the UVB at 320 nm wavelength, with a long-term average of 0.115 ± 0.095 standard deviation. These low values are typical of pristine locations in the Southern Ocean not dominated by large industrial centres. Nevertheless, episodes of high AOD's are frequent and increasing, which we attribute to biomass burning from wildfires and prescribed burning activities. Further studies are planned to examine the optical properties of these aerosols in more detail. We are hopeful that this work will add to the body of knowledge of this remote part of the Southern Hemisphere.

## ACKNOWLEDGEMENTS

The authors are grateful to the Australian Bureau of Meteorology who provided financial support for the maintenance and operations of the Hobart Brewer Station. A. Serrano thanks the R+D+i grant RTI 2018-097332-B-C22 funded by MCIN/AEI/10.13039/501100011033/ and 'ERDF A Way of Doing Europe', and the Consejería de Educación y Empleo—Junta de Extremadura for the mobility grant MOV15B036 under the program 'Becas de Movilidad al Personal Docente e Investigador de la Universidad de Extremadura y de los Centros Tecnológicos de la Comunidad Autónoma de Extremadura en centros extranjeros de

Enseñanza Superior y/o Investigación para el año 2015'. Open access publishing facilitated by University of Tasmania, as part of the Wiley - University of Tasmania agreement via the Council of Australian University Librarians.

## ORCID

*Manuel Nuñez* https://orcid.org/0000-0003-4393-1510

## REFERENCES

Alizadeh-Choobari, O., Zawar-Reza, P. and Sturman, A. (2013) Simulation of the spatial distribution of mineral dust and its direct radiative forcing over Australia. *Tellus B*, 65, 19856. https://doi.org/10.3402/tellusb.v65i0.19856.

Anderson, G., Clough, S., Kneizys, F., Chetwynd, J. and Shettle, E. (1986) *AFGL Atmospheric Constituent Profiles (0–120 km)*, Tech. Rep. AFGL-TR-86-0110. Bedford, Mass., USA: Air Force Geophysics Laboratory, Air Force Systems Command, United States Air Force: Hanscom Air Force Base, 10294.

Ångström, A. (1929) On the atmospheric transmission of the Sun radiation and on the dust in the air. *Geografiska Annaler*, 11, 156–166. https://doi.org/10.2307/519399.

Arola, A. and Koskela, T. (2004) On the sources of bias in aerosol optical depth retrieval in the UV range. *Journal of Geophysical Research.*, 109, D08209. https://doi.org/10.1029/2003JD004375.

Bais, A.F. (1997) Absolute spectral measurements of direct solar ultraviolet irradiance with a Brewer spectrophotometer. *Applied Optics*, 36, 5199–5204. https://doi.org/10.1364/AO.36.005199.

Barnes, J. and Mauersberger, K. (1987) Temperature dependence of the ozone absorption cross section at the 253.7-nm mercury line. *Journal of Geophysical Research*, 92, 14,861–14,864. https://doi.org/10.1029/JD092iD12p14861.

Bass, A.M. and Paur, R.J. (1985) The ultraviolet cross-sections of ozone: 1. The measurements. In: Zerefos, C. and Ghazi, A. (Eds.) *Atmospheric Ozone*. New York: Springer, pp. 606–616.

Bernhard, G., Evans, R.D., Labow, G.J. and Oltmans, S.J. (2005) Bias in Dobson total ozone measurements at high latitudes due to approximations in calculations of ozone absorption coefficients and air mass. *Journal of Geophysical Research*, 110, D10305. https://doi.org/10.1029/2004JD005559.

Borchers-Arriagada, N., Horsley, J.A., Palmer, A.J., Morgan, G.G., Tham, R. and Johnston, F.H. (2019) Association between fire smoke fine particulate matter and asthma-related particulate outcomes: systematic review and meta-analysis. *Environmental Research*, 179, 10877. https://doi.org/10.1016/j.envres.2019.108777.

Bucholtz, A. (1995) Rayleigh scattering calculations for the terrestrial atmosphere. *Applied Optics*, 34, 2765–2773. https://doi.org/10.1364/AO.34.002765.

Cachorro, V.E., Vergaz, R., Martin, M.J., de Frutos, A.M., Vilaplana, J.M. and de la Morena, B. (2002) Measurements and estimation of the columnar optical depth of tropospheric aerosols in the UV spectral region. *Annales Geophysicae*, 20, 565–574. https://doi.org/10.5194/angeo-20-565-2002.

Carlund, T., Kouremeti, N., Kazadzis, S.W. and Gröbner, J. (2017) Aerosol optical depth determination in the UV using a four-channel precision filter radiometer. *Atmospheric Measurement Techniques.*, 10, 905–923. https://doi.org/10.5194/amt-10-905-2017.

Carlund, T., Landelius, T. and Josefsson, W. (2003) Comparison and uncertainty of aerosol optical depth estimates derived from spectral and broadband measurements. *Journal of Applied Meteorology*, 42, 1598–1610. https://doi.org/10.1175/1520-0450(2003)042%3C1598:CAUOAO%3E2.0.CO;2.

Carvalho, F. and Henriques, D. (2000) Use of brewer ozone spectrophotometer for aerosol optical depth measurements in the ultraviolet region. *Advances in Space Research.*, 25, 997–1006. https://doi.org/10.1016/S0273-1177(99)00463-9.

Cede, A., Kazadzis, S., Kowalewski, M., Bais, A., Kouremeti, M., Blumthaler, M. and Herman, J. (2006) Correction of direct irradiance measurements of brewer spectrophotometers due to the effect of internal polarization. *Geophysical Research Letters.*, 33, L02806. https://doi.org/10.1029/2005GL024860.

Cheymol, A. and De Backer, H. (2003) Retrieval of the aerosol optical depth in the UV-B at Uccle from Brewer ozone measurements over a long time period 1984-2002. *Journal of Geophysical Research*, 108, 4800.

Clark, C. (2020) Causes of big fires in Australia: higher temperature and rainfall or more fuel? *Journal of Geoscience and Environment Protection.*, 8(8), 79–94. https://doi.org/10.4236/gep.2020.88007.

De Bock, V., De Backer, H., Mangold, A. and Delcloo, A. (2010) Aerosol optical depth measurements at 340 nm with a Brewer spectrophotometer and comparison with Cimel sunphotometer observations at Uccle, Belgium. *Atmospheric Measurement Techniques.*, 3, 1577–1588. https://doi.org/10.5194/amtd-3-2743-2010.

Diemoz, H., Eleftheratos, K., Kazadzis, S., Amiridis, V. and Zerefos, C.S. (2016) Retrieval of aerosol optical depth in the visible range with a brewer spectrometer in Athens. *Atmospheric Measurement Techniques*, 9, 1871–1888. https://doi.org/10.5194/amt-9-1871-2016.

Dowdy, A.J. (2018) Climatological variability of fire weather in Australia. *Journal of Applied Meteorology and Climatology*, 57(2), 221–234. https://doi.org/10.1175/JAMC-D-17-0167.1.

Eck, T.F., Holben, B.N., Reid, J.S., Dubovik, O., Smirnov, A., O'Neill, N.T., Slutsker, I. and Kinne, S. (1999) Wavelength dependence of the optical depth of biomass burning, urban, and desert dust aerosols. *Journal of Geophysical Research*, 104, 31333–31349. https://doi.org/10.1029/1999JD900923.

Eck, T.F., Holben, B.N., Reid, J.S., O'Neill, N.T., Schafer, J.S., Dubovik, O., Smirnov, A., Yamasoe, M.A. and Artaxo, P. (2003) High aerosol optical depth biomass burning events: A comparison of optical properties for different source regions. *Geophysical Research Letters*, 30(20), 2035. https://doi.org/10.1029/2003GL017861.

Evans, R. and Komhyr, W. (2008) *Operations Handbook – Ozone Observations with a Dobson Spectrophotometer*, WMO/GAW Report No. 183. Geneva, Switzerland: World Meteorological Organization.

Fox-Hughes, P. (2015) Characteristics of some days involving abrupt increases in fire danger. *Journal of Applied Meteorology and Climatology*, 54, 2353–2363. https://doi.org/10.1175/JAMC-D-15-0062.1.

Fox-Hughes, P., Harris, T., Lee, G., Grose, M. and Bindoff, N. (2014) Future fire danger climatology for Tasmania, Australia

using a dynamically downscaled regional climate model. *International Journal of Wildland Fire*, 23, 309–321. https://doi.org/10.1071/WF13126.

Gentilli, J. (1972) *Australian Climate Patterns*. Melbourne: Thomas Nelson, p. 285.

Gröbner, J. and Meleti, C. (2004) Aerosol optical depth in the UVB and visible wavelength range from Brewer spectrophotometer direct irradiance measurements: 1991–2002. *Journal of Geophysical Research*, 109, D09202. https://doi.org/10.1029/2003JD004409.

Hallar, A.G., Petersen, R., Andrews, E., Michalsky, J., McCubbin, I. B. and Ogren, J.A. (2015) Contributions of dust and biomass burning to aerosols at a Colorado mountain-top site. *Atmospheric Chemistry and Physics*, 15(23), 13665–13679. https://doi.org/10.5194/acp-15-13665-2015.

Hansen, J.E. and Travis, L.D. (1974) Light scattering in planetary atmospheres. *Space Science Reviews*, 16, 527–610.

Harrison, L. and Michalsky, J. (1994) Objective algorithms for the retrieval of optical depths from ground-based measurements. *Applied Optics*, 33, 5126–5132.

Harrison, L., Michalsky, J. and Berndt, J. (1994) Automated multifilter rotating shadow-band radiometer: an instrument for optical depth and radiation measurements. *Applied Optics*, 33, 5118–5125.

Holben, B.N., Tanre, D., Smirnov, A., Eck, T.F., Slutsker, I., Abuhassan, N., Newcomb, W.W., Schafer, J.S., Chatenet, B., Lavenu, F., Kaufman, Y.J., Vande Castle, J., Setzer, A., Markham, B., Clark, D., Frouin, R., Halthore, R., Karneli, A., O'Neill, N.T., Pietras, C., Pinker, R.T., Voss, K. and Zibordi, G. (2001) An emerging ground-based climatology: aerosol optical depth from AERONET. *Journal of Geophysical Research*, 106(D11), 12067–12097.

IPCC (2021). Climate change 2021: the physical science basis: summary for policymakers. *Intergovernmental Panel on Climate Change*, 31 pp.

Janjai, S., Suntaropas, S. and Nunez, M. (2009) Investigation of aerosol optical properties in Bangkok and suburbs. *Theoretical and Applied Climatology*, 96, 221–233.

Kaskaoutis, D.G., Kambezidis, H.D., Adamopoulos, A.D. and Kassomenos, P.A. (2006) On the characterization of aerosols using the Ångström exponent in the Athens area. *Journal of Atmospheric and Solar-Terrestrial Physics*, 68, 2147–2163.

Kaskaoutis, D.G., Kambezidis, H.D., Hatzianastassiou, N., Kosmopoulos, P.G. and Badarinath, K.V.S. (2007) Aerosol climatology: dependence of the Ångström exponent on wavelength over four AERONET sites. *Atmospheric Chemistry and Physics Discussions*, 7(3), 7347–7397. https://doi.org/10.5194/acpd-7-7347-2007.

Kasten, F. (1966) A new table and approximate formula for relative optical air mass. *Archives for Meteorology, Geophysics and Bioclimatology, Series B*, 14, 206–223.

Kasten, F. and Young, A.T. (1989) Revised optical air mass tables and approximation formulas. *Applied Optics*, 28, 4735–4738.

Kazadzis, S., Bais, A., Amiridis, V., Balis, D., Meleti, C., Kouremeti, N., Zerefos, C.S., Rapsomanikis, S., Petrakakis, M., Kelesis, A., Tzoumaka, P. and Kelektsoglou, K. (2007) Nine years of UV aerosol optical depth measurements at Thessaloniki, Greece. *Atmospheric Chemistry and Physics*, 7(8), 2091–2101. https://doi.org/10.5194/acp-7-2091-2007.

Kedia, S. and Ramachandran, S. (2009) Variability in aerosol optical and physical characteristics over the Bay of Bengal and the Arabian Sea deduced from Ångström exponents. *Journal of Geophysical Research*, 114, D14207. https://doi.org/10.1029/2009JD011950.

Kerr, J.B. (2002) New methodology for deriving total ozone and other atmospheric variables from Brewer spectrophotometer direct sun spectra. *Journal of Geophysical Research*, 107, 1227. https://doi.org/10.1029/2001JD001227.

Kipp and Zonen (2014). Brewer MKIII Operators Manual, 133 pp.

Kumar, K.R., Sivakumar, K., Reddy, R.R., Gopal, K.R. and Adesina, A.J. (2013) Inferring wavelength dependence of AOD and Ångström exponent over a sub-tropical station in South Africa using AERONET data: influence of meteorology, long-range transport and curvature effect. *Science of the Total Environment*, 461-462, 397–408. https://doi.org/10.1016/j.scitotenv.2013.04.095.

Kumharn, W., Rimmer, J.S., Smedley, A.R., Ying, T.Y. and Webb, A.R. (2012) Aerosol optical depth and the global brewer network: A study using UK-and Malaysia-based brewer spectrophotometers. *Journal of Atmospheric and Oceanic Technology.*, 29, 857–866. https://doi.org/10.1175/JTECH-D-11-00029.1.

Liou, K.-N. (2002) *An Introduction to Atmospheric Radiation*. London: Academic Press, p. 583.

Lopez-Solano, J., Redondas, A., Carlund, T., Rodriguez-Franco, J.J., Diémoz, H., León-Luis, S.F., Hernández-Cruz, B., Guirado-Fuentes, C., Kouremeti, N., Gröbner, J., Kazadzis, S., Carreño, V., Berjón, A., Santana-Díaz, D., Rodríguez-Valido, M., De Bock, V., Moreta, J.R., Rimmer, J., Smedley, A. R.D., Boulkelia, L., Jepsen, N., Eriksen, P., Bais, A.F., Shirotov, V., Vilaplana, J.M., Wilson, K.M. and Karppinen, T. (2018) Aerosol optical depth in the European Brewer Network. *Atmospheric Chemistry and Physics*, 18, 3885–3902. https://doi.org/10.5194/acp-18-3885-2018.

Lyons, W.A. and Cole, H.S. (1976) Photochemical oxidant transport: mesoscale lake breeze and synoptic scale aspects. *Journal of Applied Meteorology and Climatology*, 15, 733–743. https://doi.org/10.1175/1520-0450(1976)015%3C0733:POTMLB%3E2.0.CO;2.

Marenco, F. (2007) On Langley plots in the presence of a systematic diurnal aerosol cycle centered at noon: A comment on recently proposed methodologies. *Journal of Geophysical Research*, 112, D06205. https://doi.org/10.1029/2006JD007248.

Marenco, F., di Sarra, A. and DeLuisi, J. (2002) Methodology for determining aerosol optical depth from Brewer 300–320 nm ozone measurements. *Applied Optics*, 41(9), 1805–1814. https://doi.org/10.1364/AO.41.001805.

Mayer, B., Kylling, A., Emde, C., Hamann, U. and Buras, R. (2011). Libradtran user's guide, 137 pp.

McElroy, C.T. (2008). *Standard Operating Procedures Manual for the Brewer Spectrophotometer*. Environment Canada version D.01, 138 pp.

Michalsky, J., Beauhamois, M., Berndt, J., Harrison, L., Kiedron, P. and Min, Q. (1999) $O_2$-$O_2$ absorption band identification based on optical depth spectra of the visible and near-infrared. *Geophysical Research Letters*, 26, 1581–1584.

Michalsky, J., Liljegren, J. and Harrison, L. (1995) A comparison of Sun photometer derivations of total column water vapor and ozone to standard measures of same at the Southern Great

Plains Atmospheric Radiation Measurement site. *Journal of Geophysical Research.*, 100, 25,995–26,003.

Michalsky, J.J., Schlemmer, J.A., Berkheiser, W.E., Berndt, J.L., Harrison, L.C., Laulainen, N.S., Larson, N.R. and Barnard, J.C. (2001) Multiyear measurements of aerosol optical depth in the Atmospheric Radiation Measurement and Quantitative Links programs. *Journal of Geophysical Research*, 106, 12,099–12,107. https://doi.org/10.1029/2001JD900096.

Nakajima, T., Campanelli, M., Che, H., Estellés, V., Irie, H., Kim, S.-W., Kim, J., Liu, D., Nishizawa, T., Pandithurai, G., Soni, V.K., Thana, B., Tugjsurn, N.-U., Aoki, K., Go, S., Hashimoto, M., Higurashi, A., Kazadzis, S., Khatri, P., Kouremeti, N., Kudo, R., Marenco, F., Momoi, M., Ningombam, S.S., Ryder, C.L., Uchiyama, A. and Yamazaki, A. (2020) An overview of and issues with sky radiometer technology and SKYNET. *Atmospheric Measurement Techniques*, 13, 4195–4218.

Reid, J., Eck, T.F., Christopher, S.A., Hobbs, P.V. and Holben, B. (1999) Use of the Ångström exponent to estimate the variability of optical and physical properties of aging smoke particles in Brazil. *Journal of Geophysical Research*, 104, 27473–27489.

Sanchez-Romero, A., Gonzalez, J.A., Calbo, J., Sanchez-Lorenzo, A. and Michalsky, J. (2016) Aerosol optical depth in a western Mediterranean site: an assessment of different methods. *Atmospheric Research*, 174-175, 70–84. https://doi.org/10.1016/j.atmosres.2016.02.002.

Savastiouk, V. (2016). Brewer #179 calibration report. University of Tasmania, Hobart, Tas., 22 February to 1 March, 2016, 9 pp.

Savastiouk, V. (2019). Brewer #179 calibration report. University of Tasmania, Hobart, Tas., 25 February to 1 March 2016, 2019, 8 pp.

Schnaidt, F. (1938) Berechnung der relativen Schichtdicken des Wasserdampfes in der atmosphäre. *Meteorologische Zeitschrift*, 55, 296–299.

Schuster, G.L., Dubovik, O. and Holben, B.N. (2006) Ångstrom exponent and bimodal aerosol size distributions. *Journal of Geophysical Research.*, 111, D07207. https://doi.org/10.1029/2005JD006328.

Sellito, P., di Sarra, A. and Siani, A.M. (2006) An improved algorithm for the determination of aerosol optical depth in the ultraviolet spectral range from Brewer spectrophotometer observations. *Journal of Optics A: Pure and Applied Optics.*, 8, 849–855. https://doi.org/10.1088/1464-4258/8/10/005.

Smirnov, A., Holben, B.N., Eck, T.F., Dubovik, O. and Slutsker, I. (2000) Cloud-screening and quality control algorithms for the AERONET database. *Remote Sensing of Environment*, 73, 337–349.

Soni, K., Singh, S., Bano, T., Tanwar, R.S. and Nath, S. (2011) Wavelength dependence of the aerosol Ångstrom exponent and its implications over Delhi, India. *Aerosol Science and Technology*, 45(12), 1488–1498. https://doi.org/10.1080/02786826.2011.601774.

Spencer, J.W. (1971) Fourier of the sun. *Search*, 2(5), 172.

Sturman, A. and Tapper, N. (2006) *The Weather and Climate of Australia and New Zealand*. Melbourne, Australia: Oxford Univ Press, p. 520.

TFS (2016). Internal review of operations during the 2015-2016 bushfire season, Tasmanian Fire Service, 48 pp.

Torres, O., Bhartia, P.K., Herman, J.R., Syniuk, A., Ginoux, P. and Holben, B.N. (2002) A long-term record of aerosol optical depth from TOMS observations and comparison to AERONET measurements. *Journal of the Atmospheric Sciences*, 59, 398–413.

Van Heuklon, T.K. (1979) Estimating atmospheric ozone for solar radiation models. *Solar Energy*, 22, 63–68.

Wenny, B.N., Saxena, V.K. and Frederick, J.E. (2001) Aerosol optical depth measurements and their impact on surface levels of ultraviolet-B radiation. *Journal of Geophysical Research.*, 106, 17,311–17,319. https://doi.org/10.1029/2001JD900185.

WMO (2014). *The Global Atmosphere Research Programme: 25 Years of Global Coordinated Atmospheric Composition and Analyses*, WMO Report No. 1143, 46 pp.

Young, H.D. (1962) *Statistical Treatment of Experimental Data*. New York: McGraw-Hill, p. 172.

**How to cite this article:** Nuñez, M., Serrano, A., & Larson, N. R. (2023). A climatology of aerosol optical depths in the ultraviolet wavelengths for Hobart, Australia, as determined by a Brewer MKIII spectrophotometer. *International Journal of Climatology*, *43*(1), 632–649. https://doi.org/10.1002/joc.7802

## APPENDIX A

### A.1 | MONTE CARLO ERROR SIMULATION FOR BREWER AEROSOL OPTICAL DEPTH

The analysis starts with the assumption that the uncertainties may be described by a Gaussian or normalized error distribution (Young, 1962). The density distribution for any variable $x$ characterized by a standard deviation $\sigma$ and at distance of $+m$ from the origin may be expressed as:

$$f(x)=\frac{1}{\sigma\sqrt{2\pi}}e^{\frac{-(x-m)^2}{2\sigma^2}} \tag{A1}$$

and the integral of the expression forms the cumulative distribution function (CDF) with a maximum and minimum of 0 and 1 at the origin and end:

$$\phi(x)=\frac{1}{\sigma\sqrt{2\pi}}\int_{-\infty}^{x}e^{\frac{-(x-m)^2}{2\sigma^2}}dx \tag{A2}$$

A plot of $x$ versus $\phi(x)$ will vary depending on $\sigma$ and $m$. In Monte Carlo analyses, a random number is chosen between 0 and 1, which when substituted into $\phi(x)$ will provide a corresponding variable $x$. Successive execution of random numbers will yield the expected distribution in $x$ subject to $\sigma$ and $m$. As an example, $\phi(x)$ for the Rayleigh scatter coefficient $k_{\lambda R}$ is estimated. This coefficient is given as 0.9229 at 319.96 nm, the slit centre wavelength

for Brewer #179. Using an uncertainty of 1% for $k_{\lambda R}$ from Table 2, a value of $0.01 \times 0.9229 = 0.09229$ is obtained for a $1\sigma$ estimate of $k_{\lambda R}$. Substituting this estimate and $m = 0.9229$ in Equation A2, a CDF is obtained. Although the integral in Equation A2 extends from $-\infty$ to $x$, the limits of the integration can be shortened depending on the characteristics of $\sigma$ and $m$. For this example, lower and upper boundaries of $k_{\lambda R}$ can be chosen at 0.6 and 1.2, where $\phi(k_{\lambda R})$ is 0.0002 and 0.999, respectively.

The above procedure is followed for every variable in Equation A4 using generated random numbers. For the $i$th iteration, it takes the form:

$$\tau_{\lambda Ai} = \frac{-1}{m_A}\left[\ln\left(\frac{I_\lambda}{\{T_{\lambda F}\}_i * r_v * \{I_{\lambda 0}\}_i}\right) + m_0\{k_{\lambda O}\}_i\{O_3\}_i + m_R\{k_{\lambda R}\}_i\right] \tag{A3}$$

where the curly brackets denote a change from the original value: $\{Y\}_i = Y_0 + \delta Y_i$. In total $\tau_{\lambda A}$ is generated $10^4$ times, $10^3$ times for each of the 10 episodes. A deviation for this $i$th iteration may be given by:

$$\delta\tau_i = \tau_{\lambda Ai} - \tau_{\lambda A0} \tag{A4}$$

where $\tau_{\lambda A0}$ represents the original calculation without the perturbations.

The mean, $\tau_{\lambda Am}$, and standard deviation of $\tau_{\lambda A}$ ($\sigma(\tau_{\lambda A})$) can then be derived:

$$\tau_{\lambda Am} = \frac{\sum_{i=1}^{1,000} \tau_{\lambda Ai}}{1000} \tag{A5}$$

$$\sigma(\tau_{\lambda A}) = \left[\sum_{i=1}^{1,000} \frac{(\tau_{\lambda Ai} - \tau_{\lambda A0})^2}{1,000}\right]^{1/2} \tag{A6}$$

Note that Equation A6 is not a strict definition of $\sigma(\tau_{\lambda A})$ as $\tau_{\lambda A0}$ should be replaced by $\tau_{\lambda Am}$ for the relationship to be valid. In fact $\tau_{\lambda A0}$ is very close to $\tau_{\lambda Am}$, typically differing by 3 to 5%. Equation A6 is the preferred option to use here as it illustrates a clear departure from the accepted value $\tau_{\lambda A0}$.